Weak antilocalization and two-carrier electrical transport in $Bi_{1-x}Sb_x$ single crystals ($0\% \leqslant x \leqslant 17.0\%$)

Duy Minh Vu,[1,*] Wonhyuk Shon,[2,*] Jong-Soo Rhyee,[2] M. Sasaki,[3] A. Ohnishi,[3] Ki-Seok Kim,[4] and Heon-Jung Kim[1,5,†]

[1]*Department of Physics, College of Natural and Life Science, Daegu University, Gyeongbuk 38453, Republic of Korea*
[2]*Department of Applied Physics and Institute of Natural Sciences, Kyung Hee University, Yong-In, 17104, Republic of Korea*
[3]*Department of Physics, Faculty of Science, Yamagata University, Kojirakawa, Yamagata 990–8560, Japan*
[4]*Department of Physics, Pohang University of Science and Technology (POSTECH), Pohang, Gyeongbuk 37673, Republic of Korea*
[5]*Department of Materials-Energy Science and Engineering, College of Engineering, Daegu University, Gyeongbuk 38453, Republic of Korea*

Experimental investigation of the weak antilocalization (WAL) effect on the Hall resistivity is quite rare, because the WAL is known to have no influence on the Hall effect in a single-band system. We challenge this view in a system that has both electrons and holes by deriving a two-band model modified by the WAL effect and by applying it to the low-field magnetoresistance (MR) and Hall resistance (HR) of $Bi_{1-x}Sb_x$ single crystals ($0 \leqslant x \leqslant 17.0\%$). Simultaneous occurrence of a dip in MR and nonlinearity in HR suggests that the $Bi_{1-x}Sb_x$ is a rare three-dimensional system, in which WAL and two distinct charge carriers interplay. The modified two-band model describes all the main features of MR and HR that are not captured by the conventional theory. From the quantitative analysis based on the modified theory, the values of key parameters, such as carrier density and mobility of electrons and holes, are estimated. The modified two-band model provides a solid framework for understanding electrical transport phenomena of a material with strong spin-orbit interaction and multiple distinct charge carriers.

I. INTRODUCTION

Diffusive transport of electrons at low temperatures is modified by quantum interference effects, such as weak localization (WL) and weak antilocalization (WAL). These effects occur between two time-reversal trajectories of electrons that constructively interfere in a system with a weak spin-orbit interaction (SOI), giving rise to WL. In contrast, an additional π phase shift resulting from the strong coupling of spin and orbital wave functions gives rise to destructive interference and WAL in a system with strong SOI. Because the magnetic field B breaks the time-reversal symmetry required for interference, the magnetoresistance (MR) or $\rho_{xx}(B)$ is a sensitive measure for these quantum interference effects. Indeed, signatures of WL and WAL have been found as positive and negative MR, respectively, at low B in thin films [1,2], two-dimensional (2D) electron gas systems [3,4], graphene [5–8], topological insulators [9–13], and so on. Even though the influence of quantum interference effects on $\rho_{xx}(B)$ is quite well understood, that on Hall resistivity (HR) or $\rho_{xy}(B)$ has rarely been studied, because the quantum interference effects have been believed to not alter the transverse transport coefficient. However, this is true only for a single-band system. Although ρ_{xx} depends on scattering time τ, ρ_{xy} is independent of it in a single-band system; ρ_{xy} is expressed by the well-known

formula $\rho_{xy} = R_H \cdot B$, where R_H is the Hall coefficient and $R_H = -1/nec$ (n is carrier density, e is elementary charge, and c is, as usual, the velocity of light). It turns out that WL or WAL correction does not change this universal form [14,15]. Only when the system contains at least two different charge carriers distinguishable by the charge of the carrier or different scattering times, Hall resistivity ρ_{xy} explicitly depends on scattering times. This suggests that the Hall resistivity may be affected by the quantum interference effects in multi-band systems.

In 2D systems, the conductivity change $\Delta\sigma$ arising from the quantum interference effects is described by the Hikami-Larkin-Nagaoka theory [16] and its extensions [7,14,17]. In these theories, there are four fundamental length scales that determine the B dependence of $\Delta\sigma$: the mean free path l, the phase-coherence length l_ϕ, the magnetic length l_B, and the spin-orbit scattering length l_{SO}. Here l measures the average distance that an electron travels before its momentum is changed by elastic scattering; l_ϕ measures the average distance over which an electron can maintain its phase coherence. The phase coherence is usually destroyed by inelastic scattering between electron and phonon or between electrons. Thus, the ratio of l_ϕ/l divides classical and quantum diffusive regimes. In the quantum diffusive regime, where $l_\phi/l \gg 1$, electrons conserve the phase coherence even after being scattered many times. Here l_B and l_{SO} are characteristic length scales, which denote the strength of B and the SOI, respectively. For strong SOI, i.e., $l_{SO}/l < 1$, the electron wave function acquires an additional π phase without losing phase coherence after an electron adiabatically completes a closed trajectory because

---
*These authors contributed equally to this work.
†Author to whom correspondence should be addressed: hjkim76@daegu.ac.kr

of strong coupling between the spin and orbital parts of the wave function. This additional π phase is the origin of WAL in a system with strong SOI.

Despite negligible SOI, graphene can exhibit WAL because of chirality and the resultant π Berry's phase [5–7]. Because chirality in graphene originates from the equivalence of A and B sublattices, the long-range scatterers that do not mix the A and B states cannot backscatter electrons. This effect diminishes in B, resulting in an increase of resistivity with increasing B. In contrast, the point defects, which locally break sublattice degeneracy, cause intervalley scattering, which thereby leads to conventional WL. Graphene, therefore, shows competition between the WL and WAL phenomena that depend on the nature of the defects and consequently on the fundamental length scales discussed above.

Another system that contains a π Berry's phase is the topological surface state, which is composed of an odd number of massless Dirac cones. Electrons in this state have helical spin structures and acquire a π Berry's phase after completing a closed trajectory around a Fermi surface. As in graphene, this π Berry's phase leads to absence of backscattering and WAL [9–13]. In contrast to the graphene case, the WAL is robust against nonmagnetic scattering in a topological surface state, because that state is protected by time-reversal symmetry and has no valley degree of freedom. On the other hand, magnetic scatterers, which break time-reversal symmetry, weaken WAL, resulting in crossover to WL, i.e., crossover from symplectic to unitary classes [18].

Even though the quantum interference effects have been extensively explored in 2D systems, these effects are much less studied in 3D systems [19,20], partially because these effects are weaker in 3D systems than in 2D cases. Thus for systematic investigation, it is necessary to find a 3D material that exhibits pronounced quantum interference effects. A good candidate is a material with strong SOI, because strong SOI allows the quantum interference effects to be easily observable. Another problem that has been overlooked is the influence of the quantum interference on the Hall effect or ρ_{xy}. This problem is rarely explored. To fully understand this issue, it is necessary to systematically investigate both ρ_{xx} and ρ_{xy}. In this regard, the $Bi_{1-x}Sb_x$ alloy is a very suitable system, because not only does it have both electrons and holes, but it also possesses strong SOI, whose strength changes with x as does its electronic structure. Furthermore, upon increasing x, it undergoes a band character change at the hallmark topological phase transition ($x \sim 3 - 4\%$) [21–24]. Thus, electrical transport and quantum interference effects are influenced by the evolution of band structure. As a consequence, the $Bi_{1-x}Sb_x$ alloy is a system to be systematically explored for quantum interference effects, offering a clue to the relation between band topology and quantum interference effects.

The $Bi_{1-x}Sb_x$ alloy has a large region of the 3D topological insulator (TI). A 3D TI [25], which emerges in a system with strong SOI, has an inverted gap structure and Dirac-like gapless surface states. Being derived from Bi, $Bi_{1-x}Sb_x$ is the 3D TI in the region of $8.9 \leqslant x \leqslant 22.0\%$. It is a 3D TI theoretically predicted and later experimentally confirmed. The schematic phase diagram for the electronic structure of
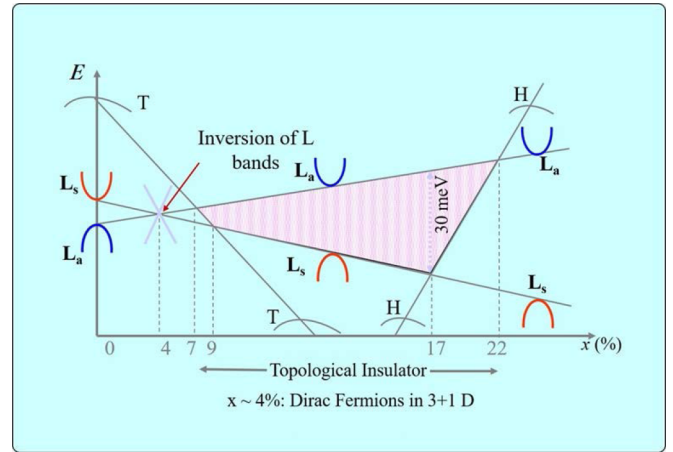

FIG. 1. Schematic phase diagram of the $Bi_{1-x}Sb_x$ system. The band at the L point undergoes a topological phase transition at $x = 3 - 4\%$, whereas the top of the band at T shows a decline with x. The insulating state is stabilized at $x \sim 7 - 9\%$, in which the Fermi level E_F is higher than the top of the T band. The present figure is adapted from Ref. [21].

$Bi_{1-x}Sb_x$ is given in Fig. 1. One remarkable feature of this alloy is a topological phase transition of the band at the L point, from a band "insulating" state at low x to a topological insulating state at high x. Bi is a well-known semimetal with electron pockets at the L point and hole pockets at the T point in the reciprocal space [22,26]. As the Sb concentration x increases, the hole band descends gradually below the Fermi energy E_F and the gap size at the L point decreases. At the critical concentration of $x \sim 3 - 4\%$, the top of the valence band touches the bottom of the conduction band, and a 3D Dirac metallic state is realized, with linear band dispersion as schematically shown in Fig. 1 [21–23]. This state is transformed into the 3D Weyl metallic state when the (pseudo) chiral degeneracy is lifted, for instance, by an external B. The 3D Weyl metallic state is robustly formed, even when the system is not precisely at the critical point, because of Zeeman splitting and the large g factor of $Bi_{1-x}Sb_x$ [17]. The existence of the 3D Weyl metallic state at $x \sim 3 - 4\%$ under the external B was confirmed by observing the chiral anomaly effect in transport phenomena [27] and the violation of Ohm's law in this Weyl metallic state [28]. By further replacing Bi with Sb, the gap at the L point reopens with inverted band structure in the wide x range of $7\% \leqslant x \leqslant 22\%$. This is a region of 3D TI. Notably, in this region impurity bands are easily formed even at tiny impurity concentrations of $\sim 10^{12}$ cm^{-3} owing to small effective mass (~ 0.01 m$_0$; m$_0$ is electron mass) and a large dielectric constant ($\sim 100 \varepsilon_0$; ε_0 is the vacuum dielectric constant) [29]. Because of this, even a very pure single crystal has significant residual conductivity. The evolution of the band structures explained above has been extensively studied and measured by angle-resolved photoemission spectroscopy [23–25,30,31]. However, the low-field (magneto) transport properties of $Bi_{1-x}Sb_x$, particularly in the 3D TI region, which might be intimately related to nontrivial band topology, are not well understood. The $Bi_{1-x}Sb_x$ alloy is a unique system that can provide important clues to how the electrical transport is influenced by nontrivial band topology and quantum

interference effects. Nontrivial band topology and multiple charge carriers are expected to interplay in this system, leading to anomalous electrical-transport phenomena with characteristic signatures in the transverse (Hall) resistivity.

We measure $\rho_{xx}(B)$ and $\rho_{xy}(B)$ at $T = 4.2$ K for -4 T $\leqslant$ $B \leqslant 4$ T over the wide x concentrations of $0\% \leqslant x \leqslant 17.0\%$. The systems in the semimetallic region ($0.0\% \leqslant x < 3.0\%$) show the transport behavior with extremely large MR, even at $B = 4$ T, because of compensation of electron and hole carriers. Here $\rho_{xx}(B)$ increases quadratically near $B = 0$, and $\rho_{xy}(B)$ shows noticeable nonlinearity [see Fig. 3(a)], which is evidence of multiple charge carriers. These features undergo a drastic change at the critical concentration of $x \sim 3.0 - 4.0\%$, where a narrow dip in $\rho_{xx}(B)$ and kinks in $\rho_{xy}(B)$ occur simultaneously at very low B [27]. The former is attributed to the WAL correction resulting from the Berry phase of 3D Dirac fermions [27]. In the TI region ($8.9 \leqslant x \leqslant 17.0\%$), $\rho_{xx}(B)$ increases with increasing B concave downward [see Fig. 3(a)]. This is distinguished from a conventional B-quadratic increase of $\rho_{xx}(B)$; $\rho_{xy}(B)$ is still nonlinear in this region. A narrow dip at the critical concentration ($x \sim 3.0 - 4.0\%$) and a concave-downward increase of $\rho_{xx}(B)$ in the TI region are clear manifestations of WAL. To quantitatively analyze both $\rho_{xx}(B)$ and $\rho_{xy}(B)$, we formulate a two-carrier model modified by the WAL effect. The main features of the experimental data are successfully described by this model. The key parameters of systems, such as the carrier density and mobility values, are estimated.

II. EXPERIMENTS AND RESULTS

We have grown $Bi_{1-x}Sb_x$ single crystals over the wide x range of $0 \leqslant x \leqslant 17.0\%$ by a Bridgeman method, as reported previously [23]. The concentrations of Sb were measured by energy dispersive x-ray analysis. We investigated five samples with $x = 0.0$, 2.3, 8.9, 11.6, and 17.0%. Temperature dependences of resistivity ρ for $Bi_{1-x}Sb_x$ single crystals were measured from 4.2 to 300 K. The $\rho_{xx}(B)$ and $\rho_{xy}(B)$ measurements were carried out by a six-probe method at 4.2 K by using a superconducting magnet with B up to 4.0 T applied along the trigonal axis and with the current perpendicular to B (binary direction).

The temperature dependence of resistivity $\rho(T)$ for $Bi_{1-x}Sb_x$ single crystals in the semimetallic ($x = 0$ and 2.3%) and gapless ($x = 3.0\%$) regions and those in the 3D TI regions ($8.9\% \leqslant x \leqslant 17.0\%$) are presented in Figs. 2(a) and 2(b), respectively. The samples in the semimetallic region are metallic; Bi has the smallest residual resistivity [$\rho(4.2$ K)] among the samples in the semimetallic and gapless regions. In these regions, the residual resistivity increases with increasing concentration of x. Notably, the $\rho(T)$ curve for the sample with $x = 3.0\%$ shows a peak at $T \sim 25$ K. A similar peak was observed in another nearly gapless system [32]. In contrast, the samples in the 3D TI region ($8.9\% \leqslant x \leqslant 17.0\%$) exhibit semiconducting $\rho(T)$ behaviors below T ~ 100 K. Another interesting observation in this region is flattening or saturation of the resistivity at low temperatures, as can be seen in the sample with $x = 11.6\%$. Here we add the extrapolation to low temperatures of the resistivity curve near 70–100 K. Clearly, this extrapolation is much higher
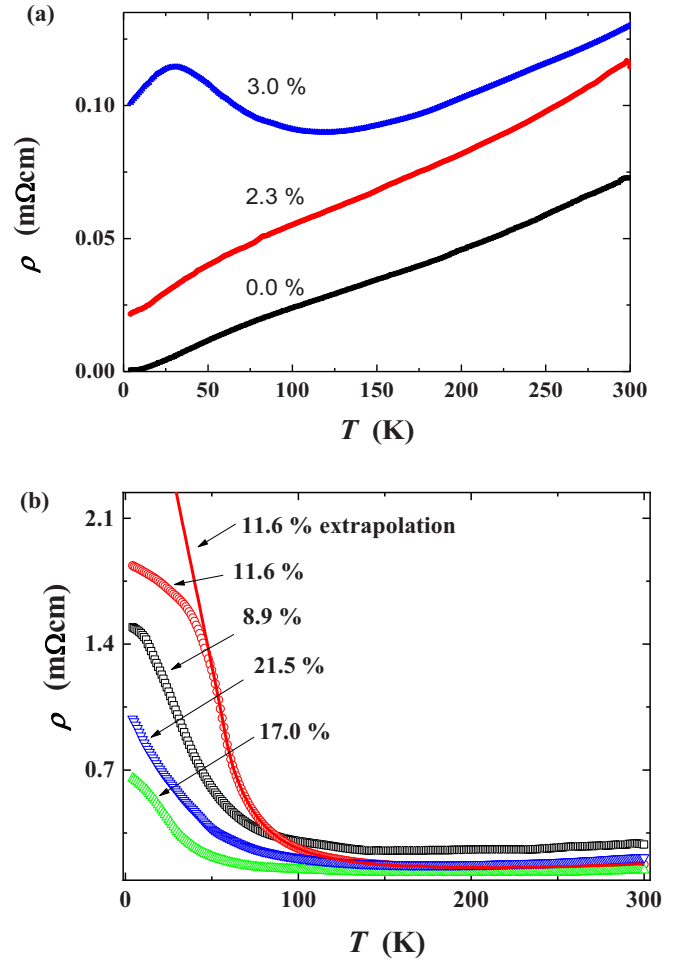

FIG. 2. Temperature dependences of resistivity ρ for $Bi_{1-x}Sb_x$ single crystals in the semimetallic and gapless regions ($0 \leqslant x \leqslant 3.0\%$) (a) and in the 3D TI region ($8.9\% \leqslant x \leqslant 17.0\%$) (b).

than the experimental resistivity data at low temperatures, suggesting an increase of conductivity at low temperatures. One possible origin for the residual conductivity is the surface states. A topological surface state could open additional conduction channels, particularly at low temperatures, giving rise to residual conductivity. However, the present samples are quite metallic, with resistivity values of only a few mΩ cm. Such low resistivity values imply dominant bulk conduction. Instead of surface states, residual conductivity can arise from the bulk effect, which is competition between two opposite tendencies. One is the drop of Fermi level E_F, upon decreasing temperature, caused by charge-carrier trapping, which reduces conductivity. On the other hand, there is much more coherence of charge carriers at low temperatures when lattice vibrations are suppressed. This is expected to increase the mean free path. The former effect dominates conductivity at higher temperature, the latter at lower temperature. Thus, coherence could result in the residual conductivity at low temperatures. In fact, the $Bi_{1-x}Sb_x$ alloy possesses a small effective mass and large dielectric constant as described above, which makes ionization energy unusually small and the Bohr radius anomalously large [29]. Even at extremely small concentrations of dopants, therefore the Bohr radius of a charge carrier overlaps
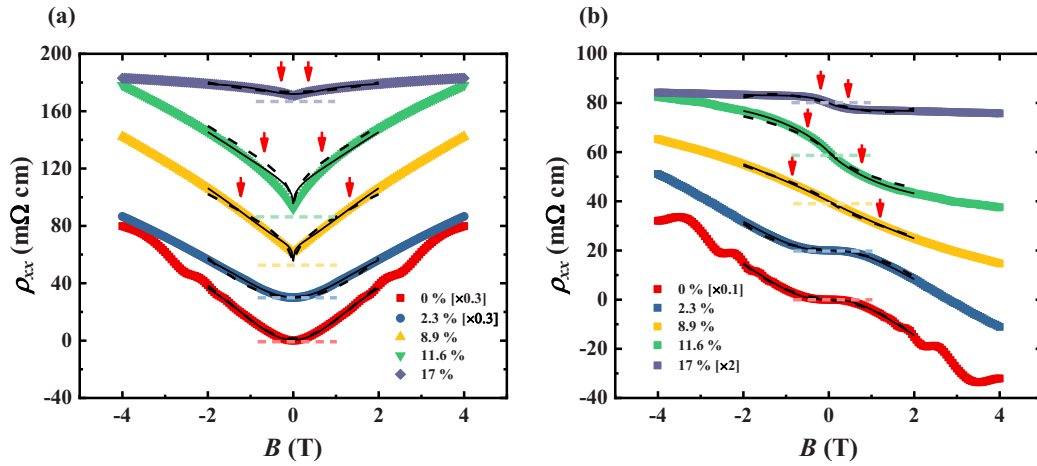
FIG. 3. (a) Magnetic field dependence of longitudinal resistivity $\rho_{xx}(B)$ and (b) that of Hall resistivity $\rho_{xy}(B)$ of the $Bi_{1-x}Sb_x$ single crystals with $x = 0.0$, 2.3, 8.9, 11.6, and 17.0%. The solid (dashed) lines represent theoretical curves that are obtained by fitting $\rho_{xx}(B)$ and $\rho_{xy}(B)$ simultaneously (independently) based on the modified two-band model. All the curves are vertically shifted for clarity. The arrows indicate the characteristic magnetic field B^*.

that of another. Thus even very clean $Bi_{1-x}Sb_x$ crystals can exhibit residual conductivity at low temperatures.

Figures 3(a) and 3(b) display $\rho_{xx}(B)$ and $\rho_{xy}(B)$, respectively, for $Bi_{1-x}Sb_x$ single crystals. The curves are vertically shifted to avoid overlap and the horizontal dashed line is the zero level of each curve. For the samples with $x = 0\%$ and 2.3%, the MR is quadratic in B in the low B region for $-0.5\,T < B < +0.5\,T$. Here MR is defined as

$$MR = \Delta\rho_{xx}/\rho_{xx} = (\rho_{xx}(B) - \rho_{xx}(0))/\rho_{xx}(0),$$

where $\rho_{xx}(B)$ and $\rho_{xx}(0)$ are resistivity values at $B = B$ and 0 T, respectively. The MR of the Bi crystal is extremely large, exceeding 4×10^5 at $B = \pm4.0\,T$, and its Shubnikov–de Haas (SdH) oscillations start at $B = \pm1\,T$. In contrast, the SdH oscillation is suppressed in the 2.3% sample, because of increased disorder in this doped system. Interestingly, compared to Bi, $\rho_{xx}(B)$ of the 2.3% sample has a narrower B-quadratic region, beyond which a B-linear tendency emerges. The $\rho_{xy}(B)$ curves of the $Bi_{1-x}Sb_x$ single crystals with $x = 0\%$ and 2.3% are not conventional, in that they are highly nonlinear. This nonlinear $\rho_{xy}(B)$ implies the existence of both electron and hole charge carriers. In fact, according to the phase diagram in Fig. 1, both electron and hole bands exist at the L and T points, respectively, in these concentrations.

Figures 3(a) and 3(b) also display the $\rho_{xx}(B)$ and $\rho_{xy}(B)$ data for the $Bi_{1-x}Sb_x$ single crystals in the 3D TI region ($8.9 \leqslant x \leqslant 17.0\%$). In this region, upon increasing B, $\rho_{xx}(B)$ increases concave downward, which differs from the $\rho_{xx}(B)$ curves at $x = 0\%$ and 2.3%. We observe no B-quadratic dependence even at very low B in the 3D TI region. Concave-downwardness strongly suggests that the B dependence of ρ_{xx} is not determined simply by conventional orbital motion of electrons. The $\rho_{xy}(B)$ curves are also quite unusual in the 3D TI region. They are highly nonlinear, particularly in the range of $-2\,T < B < 2\,T$. Here we define the inflection point in the $\rho_{xy}(B)$ curve as a characteristic field (B^*). As x increases, B^* decreases and the nonlinear region narrows. If this feature were explained by the conventional two-band model, this result would imply the mobility increase with

increasing Sb concentration. However, this is not consistent with the intuition that the sample with large x contains more disorder. Therefore, the narrowing of the nonlinear region is not reasonably explained by the conventional two-band model. It is also noted that the characteristic B defined in $\rho_{xy}(B)$ and $\rho_{xx}(B)$ roughly coincides in the same sample.

III. MODIFIED TWO-BAND MODEL

Even $\rho_{xx}(B)$ and $\rho_{xy}(B)$ curves in the semimetallic region ($x < 3.0\%$) have peculiarities that may not be explained very well by the conventional transport theory. The first notable feature is the B dependence of ρ_{xx}. Although $\rho_{xx}(B)$ is quadratic for $-2\,T < B < 2$ in Bi, that quadratic dependence does not continue beyond the region of $-0.5\,T < B < 0.5\,T$ in the 2.3% sample. Phenomenologically, $\rho_{xx}(B)$ seems to undergo crossover from quadratic to linear dependence on increasing B in the 2.3% sample, as we pointed out before. That quadratic dependence completely disappears in the 3D TI region. Instead, concave-downwardness and a dip, which we can attribute to WAL effects, develop. In this perspective, the crossover from quadratic to linear dependence may also be a manifestation of a WAL effect even in the semimetallic region. This is a quite reasonable suggestion, because the $Bi_{1-x}Sb_x$ system is expected to have stronger SOI at smaller x. On the other hand, $\rho_{xy}(B)$ is nonlinear for all x concentrations, which clearly implies the existence of electron and hole carriers in all the samples that we investigated. In fact, the existence of both electron and hole carriers is consistent with the electronic phase diagram with small electron doping for $x \leqslant 3.0\%$, where there is a single hole pocket at the T point and three electron pockets at the L point. Even in the 3D TI region ($8.9 \leqslant x \leqslant 17.0\%$), doped electrons and holes are expected to exist in the L conduction and T (or H) valence bands, respectively, because of unavoidable doping by impurities.

When electrons and holes coexist, $\rho_{xx}(B)$ and $\rho_{xy}(B)$ are described by the so-called two-band theory [33,34]. This theoretical framework, however, does not include quantum

interference effects such as WAL and WL. Therefore, a modified two-band model that takes WAL effects into account is necessary to quantitatively describe the $\rho_{xx}(B)$ and $\rho_{xy}(B)$ curves of $Bi_{1-x}Sb_x$ single crystals, because these systems have some features of WAL. In natural units ($\hbar = 1$ and $c = 1$), $\rho_{xx}(B)$ and $\rho_{xy}(B)$ in the conventional two-gap theory are given by

$$\rho_{xx}(B) = \frac{\sigma_{xx}(B)}{\sigma_{xx}(B)^2 + \sigma_{xy}(B)^2}, \tag{1}$$

$$\rho_{xy}(B) = -\frac{\sigma_{xy}(B)}{\sigma_{xx}(B)^2 + \sigma_{xy}(B)^2}, \tag{2}$$

$$\sigma_{xx}(B) = \frac{n_e e \mu_e}{1 + \mu_e^2 B^2} + \frac{n_h e \mu_h}{1 + \mu_h^2 B^2} = \frac{n_e e^2 D_e}{1 + e^2 D_e^2 B^2}$$
$$+ \frac{n_h e^2 D_h}{1 + e^2 D_h^2 B^2}, \tag{3}$$

$$\sigma_{xy}(B) = \left(\frac{n_e e \mu_e^2}{1 + \mu_e^2 B^2} - \frac{n_h e \mu_h^2}{1 + \mu_h^2 B^2} \right) B$$
$$= \left(\frac{n_e e^3 D_e^2}{1 + e^2 D_e^2 B^2} - \frac{n_h e^3 D_h^2}{1 + e^2 D_h^2 B^2} \right) B, \tag{4}$$

where σ_{xx} and σ_{xy} are magnetoconductivity and Hall conductivity, respectively, and $\mu_{e(h)}$, $n_{e(h)}$, and $D_{e(h)}$ are the mobility, carrier density, and diffusion coefficient of electron (hole), respectively. The relation between mobility $\mu_{e(h)}$ and the diffusion coefficient $D_{e(h)}$ is given by the equation $\mu_{e(h)} = e D_{e(h)}$. In the conventional two-band model, the diffusion coefficient is determined by a single scattering event and thus is given by the elastic scattering rate. According to the Drude model, the Drude conductivity σ_D is expressed by $\sigma_D = n_e e^2 D_D = \frac{n_e e^2}{m_e} \Gamma_{imp}^{-1}$, where Γ_{imp} and D_D are the transport rate and the Drude diffusion coefficient, respectively. When the WAL correction is of significance, the diffusion coefficient is modified. In $Bi_{1-x}Sb_x$, we assume that the diffusion coefficient of the electron-doped L band is renormalized by WAL because this band is more influenced by SOI. Indeed, the electron-doped L band features the topological phase transition driven by SOI. In this case, we have

$$D_e = \frac{D_D}{1 + \alpha_{WAL}/\Gamma_{imp}},$$

$$\frac{\alpha_{WAL}}{\Gamma_{imp}} = -\frac{1}{\pi n_e} \int \frac{d^3 q}{(2\pi)^3} \frac{1}{D_D q^2} = -\frac{1}{2\pi^3 n_e D_D} \int_{l_B^{-1}}^{l^{-1}} dq q^2 \frac{1}{q^2}$$

$$= -\frac{1}{2\pi^3 n_e D_D} \left(\frac{1}{l} - \frac{1}{l_B} \right) = -\frac{1}{2\pi^3 n_e D_D} \left(\frac{1}{l} - \sqrt{eB} \right)$$

$$= -\frac{1}{2\pi^3 n_e D_D} \frac{\Gamma_{imp}}{v_F} + \frac{\sqrt{eB}}{2\pi^3 n_e D_D}$$

$$= -\frac{1}{2\pi^3 n_e k_F D_D^2} + \frac{\sqrt{eB}}{2\pi^3 n_e D_D},$$

where v_F, k_F, l, and l_B are the Fermi velocity, Fermi wave vector, mean free path, and magnetic length, respectively. Here it is noted that (1) the above integration is explicitly performed in the 3D case and (2) the above calculation is

carried out in the limit of a very long phase-coherence length ($l_\phi \to \infty$) and strong SOI ($l_{SO} \to 0$). Combining the above two equations leads to the renormalized diffusion coefficient of the electron band,

$$D_e = \frac{D_D}{1 - \frac{1}{2\pi^3 n_e k_F D_D^2} + \frac{\sqrt{eB}}{2\pi^3 n_e D_D}}. \tag{5}$$

We used Eqs. (1)–(4), along with renormalized diffusion coefficient [Eq. (5)] to analyze the $\rho_{xx}(B)$ and $\rho_{xy}(B)$ data of the $Bi_{1-x}Sb_x$ samples. In fact, k_F depends on n_e, and we use the formula $k_F = (3\pi^2 n_e)^{1/3}$ that holds for a simple spherical Fermi surface as an approximation.

IV. ANALYSIS AND DISCUSSION

We use two different approaches for fitting. The first is to independently fit the $\rho_{xx}(B)$ and $\rho_{xy}(B)$ data with each set of parameters. The second is to fit $\rho_{xx}(B)$ and $\rho_{xy}(B)$ simultaneously with one common set of parameters. By comparing three sets of parameters (two from the independent fitting and one from simultaneous fitting), it is possible to estimate the valid range of each fitting parameter. As the measurements of resistivity involves at least a few tens of percent errors or larger because of uncertain sample and contact dimensions, particularly in a bulk sample, we consider the fitting reasonable if the values fitting parameters are within error ranges given by uncertain sample and contact dimensions.

The solid and dashed lines in Figs. 3(a) and 3(b) represent theoretical curves of $\rho_{xx}(B)$ and $\rho_{xy}(B)$, respectively, fit in the range for $-2\,T < B < 2\,T$ based on the modified two-band model with the WAL correction. The solid (dashed) lines are the theoretical curves obtained from the simultaneous (independent) fitting. Because the theory is applicable only in the low-field region, we restrict the fitting in this B range. For Bi, which contains the least disorder, the SdH oscillation is observed in the region of $|B| > 2T$. The fitting parameters of the analysis are the electron density n_e, the diffusion coefficient of electron D_D, the hole density n_h, and the hole mobility μ_h. The theoretical curves follow the experimental results reasonably well, and all the main characteristics of the experimental data are well captured by the theory. For instance, the theoretical curves can reproduce both the low-field B-quadratic increase and the concave downwardness of $\rho_{xx}(B)$ in the semimetallic and 3D TI regions, respectively. Furthermore, nonlinearity of $\rho_{xy}(B)$ is also well simulated by the theory. One important question here is how much the modified two-band model improves the quality of fitting compared to the results from the conventional two-band model. In fact, without the renormalization of the diffusion coefficient for the electron band [Eq. (5)], the concave downwardness of $\rho_{xx}(B)$ in the 3D TI region is not well reproduced with any reasonable parameter values. Thus, the WAL correction is quite necessary in describing the $\rho_{xx}(B)$ curves. The situation for $\rho_{xy}(B)$ is more subtle, because the conventional two-band model equally well fits the $\rho_{xy}(B)$ curves. However, when the conventional two-band model is used in fitting, an incorrect sign of charge carrier is acquired in the 3D TI region. In this case, the sign of the carrier types is the same. In addition, the hole mobility and electron mobility estimated by using
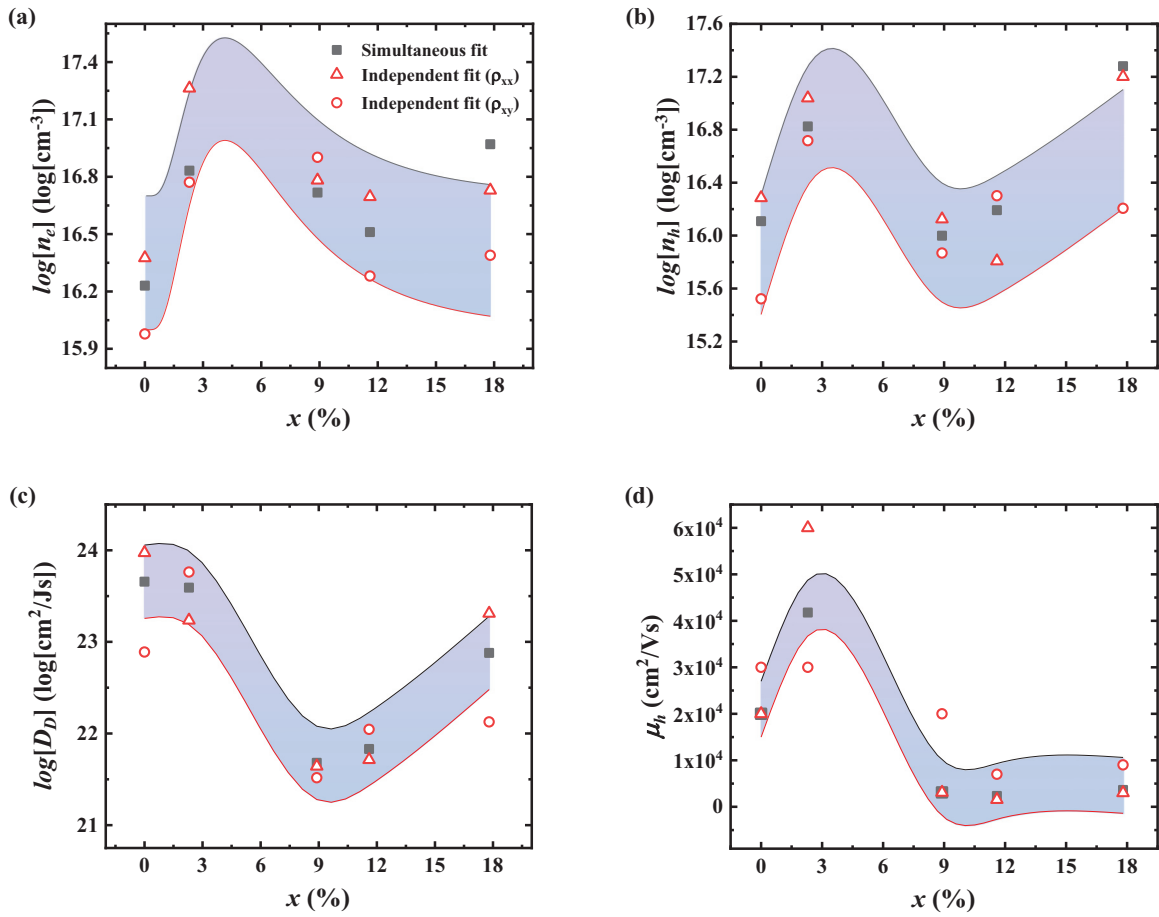
FIG. 4. (a) The electron density n_e and (b) the hole density n_h as a function of the concentration of x gained from the analysis of the modified two-band model. (c) The diffusion coefficient of electron D_D and (d) the hole mobility μ_h at different x. The shading represents the range of each parameter value.

the D_D values are different by two orders of magnitude. This situation, however, cannot occur, because this result implies a colossal disparity in cleanness of two different bands in a single system. If the sign of the charge carriers is constrained differently, the fitting curves significantly deviate from the experimental data. This demonstrates the necessity of the WAL correction even in the analysis of $\rho_{xy}(B)$ and makes the analysis of $\rho_{xx}(B)$ and $\rho_{xy}(B)$ consistent.

Figures 4(a) and 4(b) show the electron (n_e) and hole (n_h) densities, respectively, as a function of concentration x, as were deduced from the modified two-band analysis. The open (solid) symbols represent n_e and n_h acquired in the independent (simultaneous) fitting. The values of n_e and n_h are both in the range of $10^{16} - 10^{18}$ cm^{-3}. Because Bi with no doping is known to have equal numbers of electrons and holes in the range of $n_e = n_h \sim 10^{17}$ cm^{-3}, the estimated n_e and n_h values are reasonable. Despite discrepancy, the parameter values from simultaneous fitting of the $\rho_{xx}(B)$ and $\rho_{xy}(B)$ data are placed between two values from the independent fittings in most cases and their x dependences show a similar trend; both n_e and n_h reach maximum around the boundary between the semimetallic and 3D TI regions at $x \sim 3 - 4\%$. Above the maximum, n_e is slightly decreasing or is nearly constant whereas n_h increases with increasing x. The values of D_D and μ_h as a function of x, presented in Figs. 4(c) and 4(d),

respectively, also display an interesting x dependence. D_D has relatively high values in the semimetallic region. It drops by one to two orders of magnitude near the boundary between semimetallic and 3D TI regions and increases with increasing x in the 3D TI region. Similarly, μ_h undergoes a drop by a factor of four at the boundary between the semimetallic and 3D TI regions. The values of μ_h are in the order of $\sim 2 - 4$ m^2/Vs in the semimetallic region, which suggests that these systems belong to a clean regime. On the other hand, the μ_h values are considerably smaller in the 3D TI region. An assumption about a spherical Fermi surface and Eq. (5) enable one to convert D_D to the electron mobility μ_e. The estimated D_D values in the range of $10^{24} - 10^{22}$ cm^2/Js correspond to the μ_e values of $10^{-2} - 1$ m^2/Vs.

Phenomenologically, the parameters n_e, n_h, D_D, and μ_h exhibit an x dependence that changes around the boundary between the semimetallic and 3D TI regions, suggesting a fundamental change in doping characteristics. In particular, one interesting aspect in Fig. 4 is the correlation between n_e and D_D as a function of x. Below $x \sim 3 - 4\%$, D_D decreases but n_e increases with increasing x. This suggests that both impurity and dopant concentrations increase simultaneously with x, as can happen when impurities act as dopants. In contrast, above $x \sim 7 - 8\%$, n_e slightly decreases while D_D increases with x. This behavior signifies shrinkage of the
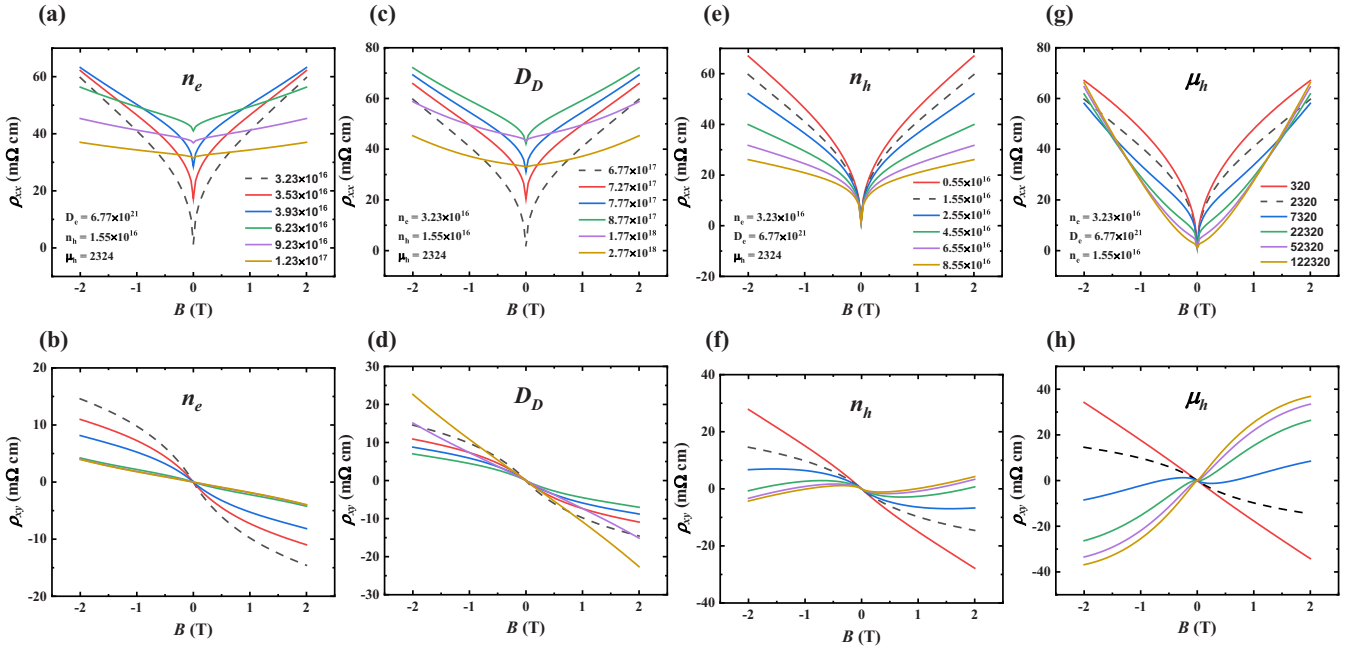
FIG. 5. Simulation of the $\rho_{xx}(B)$ and $\rho_{xy}(B)$ curves using the modified two-band model. (a)–(h) represent how the $\rho_{xx}(B)$ and $\rho_{xy}(B)$ curves change when one of the parameters is changed. (a) and (b) show the effects of electron density n_e on $\rho_{xx}(B)$ and $\rho_{xy}(B)$, respectively: (c) and (d) the effects of the electron diffusion coefficient D_D, (e) and (f) those of the hole density n_h, and (g) and (h) those of hole mobility μ_h.

electron Fermi surface. As a consequence of reduction of phase space for electrons, impurity scattering is suppressed with increasing x. This is reflected in the increase of D_D with x above $x \sim 7 - 8\%$. Clearly this differs from the behavior below $x \sim 3 - 4\%$, indicating a main influence of Sb on the band structure. For the hole band, n_h and μ_h also show interesting x dependence. Below $x \sim 3 - 4\%$, both n_h and μ_h increase with x. This simultaneous increase indicates that Sb, which is effective as an impurity in the electron band does not play a role as an impurity in the hole band. Above $x \sim 7 - 8\%$, n_h increases with x whereas μ_h stays constant. This behavior implies more dominant effect of Sb as a dopant than as an impurity that increases disorder.

To see the effects of each fitting parameter on the $\rho_{xx}(B)$ and $\rho_{xy}(B)$ curves, we simulate the $\rho_{xx}(B)$ and $\rho_{xy}(B)$ curves at different values of the parameter. Figures 5(a) and 5(b) display the effects of n_e on $\rho_{xx}(B)$ and $\rho_{xy}(B)$, respectively, and Figs. 5(c) and 5(d) those of D_D on $\rho_{xx}(B)$ and $\rho_{xy}(B)$, respectively. When n_e decreases at fixed D_D, n_h, and μ_h, the quadratic increase in $\rho_{xx}(B)$ evolves into concave-downward increase through the tiny dip at the low B region. At higher B, the concave downwardness appears below $n_e < 6.23 \times 10^{16}$ cm^{-3}. The concave downwardness remarkably differs from the B-quadratic increase of $\rho_{xx}(B)$ observed in a metal in the absence of the WAL correction. In the parameter ranges that we investigate, the dip and concave downwardness is more pronounced at smaller n_e. On the other hand, $\rho_{xy}(B)$ is nonlinear, as expected, and the amplitude of this nonlinear S-shape becomes smaller with increasing n_e. Notably, the changes of the $\rho_{xx}(B)$ and $\rho_{xy}(B)$ curves caused by D_D look very similar to the effect of n_e. Compare [Figs. 5(a) and 5(b)] with [Figs. 5(c) and 5(d)]. This can be understood by considering the dependence of D_e on n_e and D_D [Eq. (5)].

Because D_e is a function of both n_e and D_D, a change of D_D can change the $\rho_{xx}(B)$ and $\rho_{xy}(B)$ curves much as that of n_e does.

Even though only the electron band is corrected by WAL, the hole density n_h and mobility μ_h influence the $\rho_{xx}(B)$ and $\rho_{xy}(B)$ curves drastically. This change of $\rho_{xx}(B)$ and $\rho_{xy}(B)$ by n_h and μ_h is demonstrated in Figs. 5(e)–5(h). Upon increase of n_h, $\rho_{xx}(B)$ at high B is flattened. This change leaves a smaller dip feature at the low B region, which gets smaller at higher n_h. The influence of n_h on $\rho_{xy}(B)$ is also interesting. As n_h increases, $\rho_{xy}(B)$ is more curved and overall slope change occurs at high B region, whereas the slope at the low B region is still negative. The section in $\rho_{xy}(B)$ with positive slope widens. Thus, the slope at $B = 2$ T changes from the negative value at $n_h = 0.55 \times 10^{16}$ cm^{-3} to positive at $n_h = 1.55 \times 10^{16}$ cm^{-3}. The effects of the μ_h parameter on $\rho_{xx}(B)$ and $\rho_{xy}(B)$, presented in Figs. 5(g) and 5(h), respectively, are also nontrivial. The concave downwardness of $\rho_{xx}(B)$ evolves into the quadratic MR with a tiny dip with μ_h increasing. The $\rho_{xy}(B)$ curve also shows drastic μ_h dependence as $\rho_{xx}(B)$ does. The $\rho_{xx}(B)$ curve is almost linear at $\mu_h = 320$ cm^2/Vs with overall negative slope and become curved at $\mu_h = 2320$ cm^2/Vs. From $\mu_h = 7320$ cm^2/Vs, the slope at the high B region changes into negative value. Further increase of μ_h leads to change of the curvature at the high B region of $\rho_{xy}(B)$. Relatively large values of μ_h make overall slope of the $\rho_{xy}(B)$ curve positive as n_h does. This indicates dominant contribution of hole carriers at relatively high values of μ_h and n_h.

V. CONCLUSION

We have systematically studied the MR and HR of Bi$_{1-x}$Sb$_x$ single crystals over the wide Sb concentration range

of x ($0 \leqslant x \leqslant 17.0\%$) at 4.2 K and with B up to 4.0 T. These transport quantities were quite unconventional because of the weak antilocalization and two-carrier transport. MR shows not conventional B-quadratic behavior, but a dip at low B in the 3D topological insulating region. On the other hand, HR is nonlinear in B with an S-shape. The former and the latter can be mainly attributed to weak antilocalization and two-band effects, respectively. To understand the MR and HR of $Bi_{1-x}Sb_x$ single crystals based consistently on weak antilocalization and two-band effects, we formulated a two-band model modified by weak antilocalization. We applied it to analyze MR and HR data, and the modified two-band model successfully described all the main features of the experimental data that are not captured by the conventional two-band theory. This suggests that the $Bi_{1-x}Sb_x$ alloy is a system that shows the interplay of weak antilocalization and two distinct charge carriers. As a transport theory that includes not only two-carrier transport but also weak antilocalization, the modified two-band model offers a solid framework to understand the electrical properties of a material with strong spin-orbit interaction and multiple charge carriers. Our study also provides a clue how to incorporate the quantum interference effect into a transport theory, particularly in the regime of strong spin-orbit interaction.

[1] J. J. Lin and N. Giordano, Phys. Rev. B **35**, 1071 (1987).

[2] G. Bergmann, Phys. Rev. B **25**, 2937(R) (1982).

[3] D. J. Bishop, R. C. Dynes, and D. C. Tsui, Phys. Rev. B **26**, 773 (1982).

[4] T. Koga, J. Nitta, T. Akazaki, and H. Takayanagi, Phys. Rev. Lett. **89**, 046801 (2002).

[5] F. V. Tikhonenko, A. A. Kozikov, A. K. Savchenko, and R. V. Gorbachev, Phys. Rev. Lett. **103**, 226801 (2009).

[6] X. Wu, X. Li, Z. Song, C. Berger, and W. A. de Heer, Phys. Rev. Lett. **98**, 136801 (2007).

[7] E. McCann, K. Kechedzhi, V. I. Fal'ko, H. Suzuura, T. Ando, and B. L. Altshuler, Phys. Rev. Lett. **97**, 146805 (2006).

[8] S. V. Morozov, K. S. Novoselov, M. I. Katsnelson, F. Schedin, L. A. Ponomarenko, D. Jiang, and A. K. Geim, Phys. Rev. Lett. **97**, 016801 (2006).

[9] J. Chen, H. J. Qin, F. Yang, J. Liu, T. Guan, F. M. Qu, G. H. Zhang, J. R. Shi, X. C. Xie, C. L. Yang, K. H. Wu, Y. Q. Li, and L. Lu, Phys. Rev. Lett. **105**, 176602 (2010).

[10] H.-T. He, G. Wang, T. Zhang, I.-K. Sou, G. K. L Wong, J.-N. Wang, H.-Z. Lu, S.-Q. Shen, and F.-C. Zhang, Phys. Rev. Lett. **106**, 166805 (2011).

[11] M. Liu, J. Zhang, C.-Z. Chang, Z. Zhang, X. Feng, K. Li, K. He, Li-li Wang, Xi Chen, Xi Dai, Z. Fang, Qi-Kun Xue, X. Ma, and Y. Wang, Phys. Rev. Lett. **108**, 036805 (2012).

[12] H.-Z. Lu, J. Shi, and S.-Q. Shen, Phys. Rev. Lett. **107**, 076801 (2011).

[13] Y. S. Kim, M. Brahlek, N. Bansal, E. Edrey, G. A. Kapilevich, K. Iida, M. Tanimura, Y. Horibe, S.-W. Cheong, and S. Oh, Phys. Rev. B **84**, 073109 (2011).

[14] B. L. Altshuler, D. Khmel'nitzkii, A. I. Larkin, and P. A. Lee, Phys. Rev. B **22**, 5142 (1980).

[15] H. Fukuyama, J. Phys. Soc. Jpn. **49**, 644 (1980).

[16] S. Hikami, A. I. Larkin, and Y. Nagaoka, Prog. Theor. Phys. **63**, 707 (1980).

[17] C. W. J. Beenakker and H.V. Houten, Solid State Phys. **44**, 1 (1991).

[18] F. Evers and A. D. Mirlin, Rev. Mod. Phys. **80**, 1355 (2008).

[19] A. Kawabata, Solid State Commun. **34**, 431 (1980).

[20] A. Kawabata, J. Phys. Soc. Jpn. **49**, 628 (1980).

[21] B. Lenoir, M. Cassart, J.-P. Michenaud, H. Scherrer, and S. Scherrer, J. Phys. Chem. Solids **57**, 89 (1996).

[22] L. Fu and C. L. Kane, Phys. Rev. B **76**, 045302 (2007).

[23] H. Guo, K. Sugawara, A. Takayama, S. Souma, T. Sato, N. Satoh, A. Ohnishi, M. Kitaura, M. Sasaki, Q.-K. Xue, and T. Takahashi, Phys. Rev. B **83**, 201104(R) (2011).

[24] F. Nakamura, Y. Kousa, A. A. Taskin, Y. Takeichi, A. Nishide, A. Kakizaki, M. D'Angelo, P. Lefevre, F. Bertran, A. Taleb-Ibrahimi, F. Komori, S.-ichi Kimura, H. Kondo, Y. Ando, and I. Matsuda, Phys. Rev. B **84**, 235308 (2011).

[25] M. Z. Hasan and C. L. Kane, Rev. Mod. Phys. **82**, 3045 (2010).

[26] Ph. Hofmann, J. E. Gayone, G. Bihlmayer, Yu. M. Koroteev, and E. V. Chulkov, Phys. Rev. B **71**, 195413 (2005).

[27] H.-J. Kim, K.-S. Kim, J. F. Wang, M. Sasaki, N. Satoh, A. Ohnishi, M. Kitaura, M. Yang, and L. Li, Phys. Rev. Lett. **111**, 246603 (2013).

[28] D. Shin, Y. Lee, M. Sasaki, Y. H. Jeong, F. Weickert, J. B. Betts, H.-J. Kim, K.-S. Kim, and J. Kim, Nat. Materials **16**, 1096 (2017).

[29] B. Lenoir, H. Scherrer, and T. Caillat, Semiconduct. Semimet. **69**, 101 (2001).

[30] D. Hsieh, D. Quin, L. Wary, Y. Xia, Y. S. Hor, R. J. Cava, and M. Z. Hasan, Nature (London), **452**, 970 (2008).

[31] A. Nishide, A. A. Taskin, Y. Takeichi, T. Okuda, A. Kakizaki, T. Hirahara, K. Nakatsuji, F. Komori, Y. Ando, and I. Matsuda, Phys. Rev. B **81**, 041309(R) (2010).

[32] M. Sasaki. A. Ohnishi, N. Satoh, K. Suga, K. Kindo, K. Inomata, H. Ebina, and S. J. Lee, Phys.Procedia **3**, 1305 (2010).

[33] M. Sasaki, K.-M. Kim, A. Ohnishi, M. Kitaura, N. Tomita, V. A. Kulbachinskii, Ki-Seok Kim, and Heon-Jung Kim, Phys. Rev. B **92**, 205121 (2015).

[34] J.-F. Wang, M. Yang, L. Li, M. Sasaki, A. Ohnishi, M. Kitaura, K.-S. Kim, and H.-J. Kim, Phys. Rev. B **89**, 035137 (2014) .